Journal of the Taiwan Institute of Chemical Engineers 122 (2021) 201–209

Contents lists available at ScienceDirect

Journal of the Taiwan Institute of Chemical Engineers

journal homepage: www.elsevier.com/locate/jtice

Photocatalytic behavior of $Ba(Sb/Ta)_2O_6$ perovskite for reduction of organic pollutants: Experimental and DFT correlation

Madhuri S. Patil[a,b], Narasimharao Kitchamsetti[a], Sameena R. Mulani[a], Sachin R. Rondiya[c], Nishad G. Deshpande[d], Ranjit A. Patil[e], Russell W. Cross[c], Nelson Y. Dzade[c], Kirankumar K. Sharma[b], Pramod S. Patil[b], Yuan-Ron Ma[e], Hyung Koun Cho[d], Rupesh S. Devan[a,*]

[a] Department of Metallurgy Engineering & Materials Science, Indian Institute of Technology Indore, Simrol, Indore 453552, India
[b] School of Nanoscience and Technology, Shivaji University, Kolhapur, Maharashtra 416004, India
[c] School of Chemistry, Cardiff University, Cardiff, Wales CF10 3AT, United Kingdom
[d] School of Advanced Materials Science and Engineering, Sungkyunkwan University, 2066, Seobu-ro, Jangan-gu, Suwon-si, Gyeonggi-do 16419, Republic of Korea
[e] Department of Physics, National Dong Hwa University, Hualien 97401, Taiwan

ARTICLE INFO

Article History:
Received 25 November 2020
Revised 2 April 2021
Accepted 18 April 2021
Available online 11 May 2021

Keywords:
$Ba(Sb/Ta)_2O_6$ perovskite
DFT
Photocatalytic dye degradation
XPS
Organic pollutant

ABSTRACT

We have synthesized closely packed hexagonal 2D plates and clustered nanoparticle morphologies of $Ba(Sb/Ta)_2O_6$ (BSTO) perovskite via the polymerizable complex method for photocatalytic dye degradation activities. The BSTO crystallized in a hexagonal structure. The presence of Ba^{2+}, Sb^{5+}, Ta^{5+}, and O^{2-} chemical states identified from XPS confirmed the formation of mixed $Ba(Sb/Ta)_2O_6$ phase accompanied with a minor amount of TaO_x. Furthermore, BSTO showed excellent photocatalytic activity for the degradation of various organic dyes. The kinetic studies revealed 65.9%, 77.3%, 89.8%, and 84.2%, of Crystal Violet (CV), Methylene Blue (MB), Rhodamine blue (RhB), and Methylene Orange (MO), respectively, after irradiation of 180 min without using a cocatalyst. The formation of O_2^- and OH^-surface radicals, which are believed to facilitate the degradation of the dyes, are unveiled through first-principles Density Functional Theory (DFT) calculations and scavenging studies. Our results suggest that BSTO holds promise as an excellent photocatalyst with better degradation efficiency for various organic dyes.

1. Introduction

Access to clean and safe drinking water is essential for human health and wellbeing, and lies at the heart of Sustainable Development Goal 6: 'i.e., ensure availability and sustainable management of water and sanitation for all.' However, human activities and pharmaceutical and textile industrial processes have introduced dangerous contaminants in water systems, raising serious health concerns. Therefore, there is an urgent need to develop efficient water treatment technologies to provide potable water for society. Various physical, chemical, and biological treatments for water purification have been explored with limited efficiencies [1,2]. However, recent advancements in photocatalysis technologies have enabled the development of highly effective materials capable of degradation of various pharmaceutical compounds and the development of visible-light photocatalysts [3]. Photocatalytic water treatment has many advantages over other water purification methods as it is a highly eco-friendly, low-cost, reusable, and highly efficient method. Photocatalysis has also served the needs of energy consumption and environmental pollutant remediation through various processes such as water splitting, degradation of organic pollutants, and reduction of heavy metals and CO_2 gas.

Advanced oxidation processes activate the photocatalytic material by light energy and generate electron-hole pairs responsible for generating surface hydroxyl and other radicals, which further react with organic pollutants such as dyes, herbicides, and pesticides to degrade them through the oxidation process [4]. TiO_2 is the most investigated photocatalytic material, but the low adsorption of hydrophobic pollutants, high aggregation nature, complications with separation and recovery, and photocatalytic activity in only the UV region [5,6] necessitates the rational design and development of other metal oxides to gain better photocatalytic activities for dye degradation. Therefore, to overcome the limitations of TiO_2, previous

* Corresponding author.
E-mail address: rupesh@iiti.ac.in (R.S. Devan).

https://doi.org/10.1016/j.jtice.2021.04.032

investigations have partially modified and/or replaced TiO_2 with other semiconducting oxides such as WO_3, ZnO, SnO_2, Fe_2O_3, etc., [7] polymeric compounds like Polyaniline (PANI) and Polyvinylidene-fluoride (PVDF), [8,9] and carbonaceous materials such as graphene, CNT, and g-C_3N_4, etc. [10].

In recent years, the development of new mixed metal oxides for photocatalytic degradation of various organic dyes is of prime consideration. The unique structural and electrical properties of various tantalates, niobates, antimonates, and titanates are expected to provide better stability, hence attracting attention to a large extent for the photocatalytic activity for water splitting and degradation of dyes. The corner shared octahedral arrangement of TaO_6 exhibiting a bond angle of 180° in the Ta-O-Ta structure should facilitate e^- - h^+ pair separation and decrease their recombination rate, resulting in enhanced photocatalytic carrier generation. Therefore, the tantalates such as $NaTaO_3$, $KTaO_3$, $Ba_4Ta_2O_9$, $Ba_5Ta_4O_{15}$, $BaTa_2O_6$, $BaTa_4O_{11}$and Rh/Ir doped $BaTa_2O_6$[11–15] have delivered better photocatalytic activities in water splitting. Nevertheless, reports in the literature focusing on exploring their dye degradation studies are very limited. On the other hand, the distorted Sb-O octahedral structure in $BaSb_2O_6$ is shown to be active towards photocatalysis due to its lattice distortion in magnitude and direction [16]. The antimonates such as $ZnSb_2O_6$, $CdSb_2O_6$, and $BaSb_2O_6$ [17,18] are explored for the photocatalytic degradation of RhB. Recently, Chen et al. [16] reported the effect of the active surface area of $BaSb_2O_6$ on the photocatalytic degradation of RhB, but H_2O_2 was found to influence the degradation rate mostly. Moreover, the hydrogen-related defects in the hydrothermally synthesized $BaTa_2O_6$ adversely affected the photocatalytic degradation of RhB in an aqueous solution under UV radiation [14]. $ZnSb_2O_6$ delivered 95% degradation of RhB after photocatalytic irradiation of 150 min. However, doping of Tb^{3+} (1.2%) and Eu^{3+} (0.8%), considered for dual functionality, did not exhibit any significant improvement in the degradation ability of $ZnSb_2O_6$ [17]. The doping of Ir and La has been explored to enhance the photocatalytic activities, but studies are limited to H_2 evoluation and not to dye degradation activities [19]. On the other hand, the double perovskites such as Ba_2RBiO_6 (R = Ce, Sm, Eu, Gd, Dy) delivered the bandgap in the range of 1.60 to 1.71 eV and confirmed photocatalytic dye degradation activities under visible light irradiation. Nevertheless, all those double perovskites have shown sluggish photocatalytic degradation of MB dye (i.e., ~ 74% in 8 h) [20]. To the best of our knowledge, no research group has explored the photocatalytic activity either after combining the $BaTa_2O_6$ (BTO) and $BaSb_2O_6$ (BSO) or partial replacement of Sb and Ta. The distinctive larger bandgap of both BTO (i.e., 3.85 to 4.2 eV) and BSO (3.8 to 4.7 eV) [12,18,21,22] has the potential to utilize a broader spectrum for photocatalytic activity after combining or partially replacing Sb and Ta. Therefore, in the present study, we have explored the photocatalytic activity of $Ba(Ta/Sb)_2O_6$ in the degradation of aqueous Methylene Orange (MO), Methylene Blue (MB), Crystal Violet (CV), and Rhodamine Blue (RhB) without the utilization of any cocatalyst.

The $Ba(Sb/Ta)_2O_6$ perovskite synthesized by the polymerizable complex method is investigated for the photocatalytic degradation of MO, MB, CV, and RhB dyes at room temperature. The structural properties were investigated from X-ray diffraction. The surface morphologies and chemical composition of the BSTO were explored using field emission scanning electron microscopy (FESEM) and x-ray photoemission spectroscopy (XPS), respectively. The effect of BSTO concentration on the photocatalytic degradation of MB was investigated systematically by irradiation under a xenon lamp (300 W) and continued further for MO, CV, and RhB. The BSTO perovskite delivered the best photocatalytic activity in the degradation of RhB without using any cocatalyst. Theoretical insights into the electronic structure of the BSTO material are provided, and the active sites for the formation of O_2^- and OH^-surface radicals to facilitate the degradation of the dyes are predicted.

2. Experimental techniques

2.1. Synthesis and characterization

The synthesis of BSTO was carried out via polymerizable complex method using barium barbonate ($BaCO_3$, ≥ 99%, Sigma Aldrich), tantalum chloride ($TaCl_5$, 99.99%, Sigma Aldrich), and antimony chloride ($SbCl_3$, 99.95% Sigma Aldrich) as starting materials. The anhydrous methanol was used as a solvent for dissolving precursors. The stoichiometric amount of the 0.1 M $BaCO_3$, 0.05 M $SbCl_3$, and 0.05 M $TaCl_5$ were dissolved in 20 ml of anhydrous methanol (CH_3OH, 99.8%, Sigma Aldrich) at room temperature, and 0.05 M citric acid ($C_6H_8O_7$, ≥ 99.5%, Sigma Aldrich) was added afterward under constant starring. Furthermore, the 40 ml ethylene glycol ($C_2H_6O_2$, 99.8%, Sigma Aldrich) was added to the solution as a polymerization agent and reacted at 130°C to obtain the viscous whitish gel. The viscous gel was dried initially at 350°C and annealed further at ~1200°C for 10 h to obtain $Ba(Sb/Ta)_2O_6$ (i.e., BSTO) powder. The surface morphological features of BSTO are confirmed from field emission scanning electron microscopy (FESEM, JEOL JSM-7610 F Plus). X-ray diffraction (D2-Phaser Bruker, Cu-Kα, λ = 1.5406 Å) was utilized to confirm the crystal structure and identify the phase of the BSTO. The chemical states and electronic properties are confirmed using X-ray photoelectron spectroscopy (XPS, Thermo Scientific Inc. Al-Kα) with microfocus monochromated Al Kα X-rays. UV-Visible diffuse reflectance spectra recorded using a UV-Visible spectrophotometer (Shimadzu, UV-2600) in the wavelength range of 200 to 800 nm to evaluate the bandgap. Also, the dye degradation study was carried out under the xenon lamp in a chemical reactor.

The photocatalytic activities of the BSTO were analyzed by the degradation of various dyes under the xenon Lamp (λ = 100 to 1800 nm) in Photo-Chem Reactor. The photocatalytic activity was tested on MB, RhB, MO, and CV dyes. Initial optimization on the degradation activities of BSTO was carried out with variation in the concentration of the MB (i.e., 10, 20, and 30 mg/L). The dye solution was maintained in the dark for 30 min. to obtain adsorption-desorption equilibrium and further irradiated under a xenon lamp. The irradiated solution was tested under UV–Vis light at regular intervals using a UV–Vis spectrophotometer to attain maximum degradation of the dye under observation. The absorption peak at λ_{max} signifies the dye concentration remained in solution after irradiation of UV- Visible light. The best optimization concentration (i.e., 10 mg/L for MB) was subjected further for the degradation studies of RhB, MO, and CV dyes

2.2. DFT analysis

The electronic structure calculations were performed based on density functional theory (DFT) methodology, as implemented in the Vienna Ab initio Simulation Package (VASP) [23]. The interactions between the core and valence electrons were treated using the Project Augmented Wave (PAW) method [24]. The electronic wave functions are expanded on a plane-wave basis set with cut-off energy of 600 eV. Geometry optimizations were performed using the conjugate-gradient algorithm until the residual Hellmann–Feynman forces on all relaxed atoms reached 10^{-3} eV/Å. The electronic exchange-correlation potential was calculated using the Perdew–Burke–Ernzerhof (PBE) generalized gradient approximation (GGA) functional [25]. Long-range vdW interactions were accounted for using the Grimme DFT-D3 scheme [26]. The bulk BSTO was modeled in the hexagonal structure (*P6/mmm* [191]). A 3 × 3 × 9 Monkhorst-Pack k-point mesh used to sample the Brillouin zone. A full unit cell relaxation yield the lattice parameters of BSTO to be a = 21.328 Å and c = 3.957 Å, which compares closely with the experimental lattice parameter of the $BaTa_2O_6$ counterpart (a = 21.116 Å and c = 3.9157 Å) [27]. The screened hybrid functional HSE06 [28] with an exchange value of 30% was used to predict the

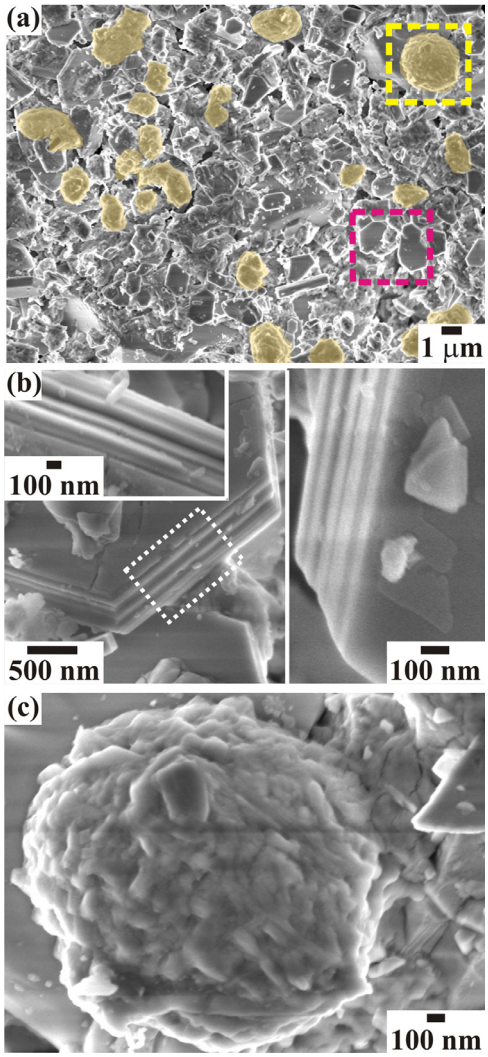

Fig. 1. FESEM images of BSTO material identifying (a) stacking of 2D hexagonal nanoplates and microspheres of clustered nanoparticles (identified yellow) morphologies, (b) hexagonal 2D nanoplates stacked over one other, and (c) microsphere consisted of clustered nanoparticles identified red and yellow in Fig (a). The inset (b) shows the high magnification image of close-packed stacks of hexagon layers from the marked white region. (For interpretation of the references to color in this figure legend, the reader is referred to the web version of this article.).

electronic density of states (DOS) and the bandgap. The BSTO(100) surface was used to characterize the adsorption characteristics of O_2 and H_2O molecules. A 5 × 5 × 1 *k*-point was used for the surface calculations. Bader charge analysis [29] was used to quantify charge transfers between the BSTO(100) surface and the adsorbing molecules.

3. Results and discussion

The surface morphological aspects of BSTO are confirmed from FESEM images shown in Fig. 1. Fig. 1(a) illustrates that the prepared material is composed of two different morphologies, i.e., two-dimensional (2D) hexagonal plates and clusters of nanoparticles in the form of spheres. The reason for the formation of two different morphologies is unknown, but one of the possible reasons might be the segregation of Sb and Ta to form $BaSb_2O_6$ and $BaTa_2O_6$ independent phases. The hexagonal plates are distributed uniformly in large quantities compared to clustered nanoparticles throughout the sample (highlighted in yellow). The hexagonal plates are of size ~ 0.5 to 2 μm. The high-magnification FESEM images in Fig. 1(b) of the portion marked red in Fig. 1(a) confirm the formation of hexagonal 2D plates with clearly visible textural boundaries. The hexagonal plates are composed of intact stacking of 6–7 layers, each of thickness approximately < 100 nm. The clustered features are partially spherical shaped with a diameter in the range of 1 to 3 μm. Fig. 1(c) shows the high magnification FESEM image of the perfectly spherical cluster of nanoparticles from the portion marked yellow in Fig. 1(a). The spherical particle comprises irregularly shaped nanoparticles with one of the dimensions in the range of 100 to 150 nm.

The morphology as well as the lattice structure of the $Ba(Sb/Ta)_2O_6$ sample were analyzed by TEM measurements. The TEM image of the $Ba(Sb/Ta)_2O_6$ sample along with the lattice fringes is shown in Fig. 2(a) and (b). It revealed the formation of a stacked structure surrounded by the clustered particles, which is identical to the FESEM studies (Fig. 1). The HRTEM image (Fig. 2(b)) clearly revealed the polycrystalline nature of the sample. Moreover, it indicated clear domain boundaries with lattice fringes having different orientations. On the basis of the calculations of the lattice spacing and the analysis of its orientation, it is found that the $Ba(Sb/Ta)_2O_6$ possibly consists of combined mixed phases of $BaTa_2O_6$ [lattice direction (411) with lattice spacing 0.28 nm] and $BaSb_2O_6$ [lattice direction (200) with lattice spacing 0.22 nm], which are consistent with the XRD data (Fig. S1). Having similar crystal structure and matching peak positions

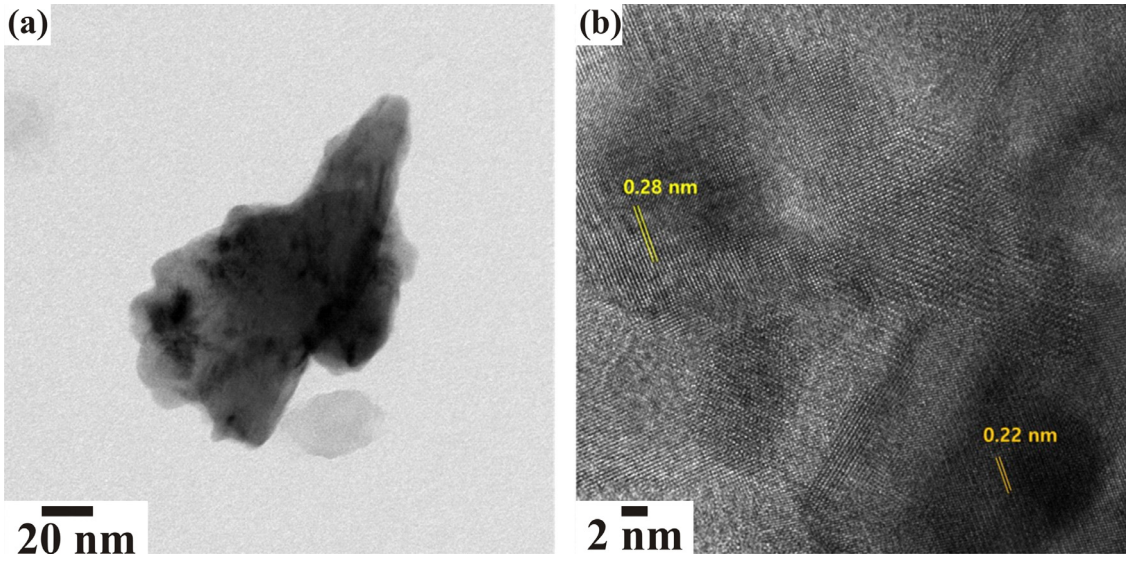

Fig. 2. (a) TEM and (b) HRTEM image of the $Ba(Sb/Ta)_2O_6$ sample showing clear lattice fringes.

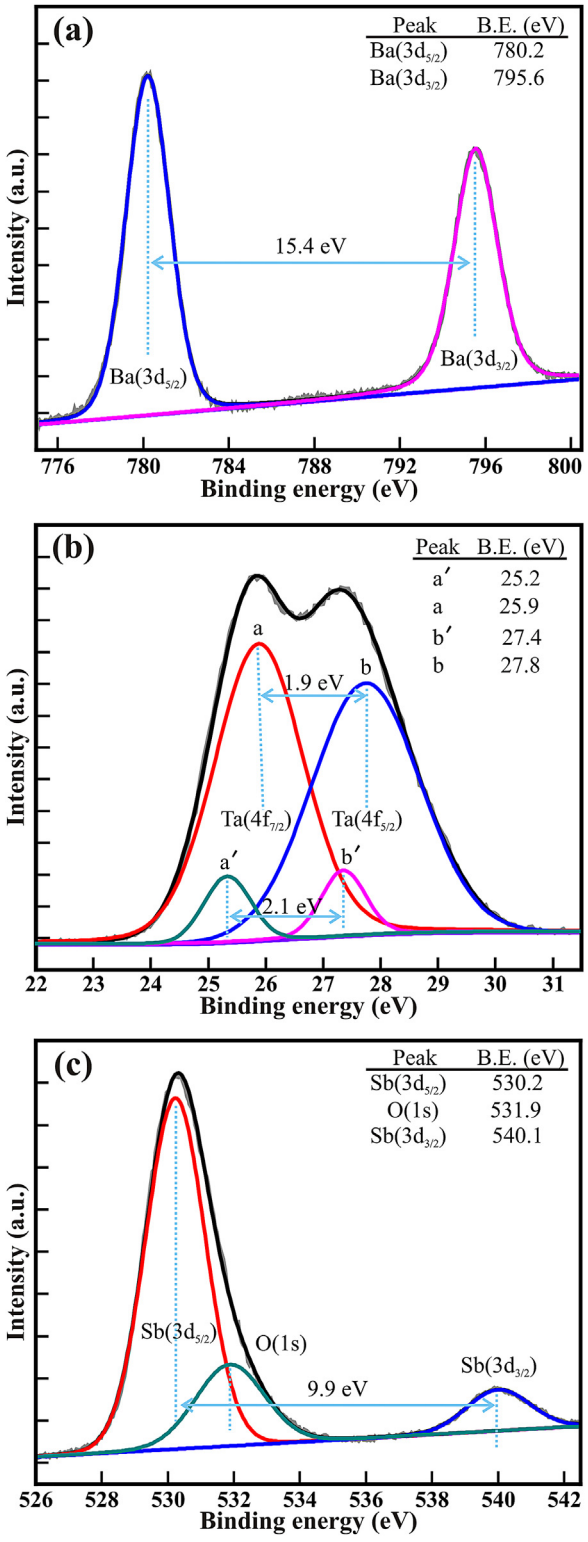

Fig. 3. High resolution XPS spectra of (a) Ba(3d), (b) Ta(4f), and (c) Sb(3d) core levels of BSTO perovskite. The XPS spectra were deconvoluted via the Voigt curve function within the Shirley background.

between $BaTa_2O_6$ and $BaSb_2O_6$, the sample indicates a synergetic Ba $(Sb/Ta)_2O_6$ mixture.

The crystal structure, figure print of the materials is analyzed from the XRD pattern. The XRD spectrum in Fig. S1 was recorded after annealing BSTO at 1200 °C for 10 hr, showing sharp and intense peaks, and confirmed the good crystallinity of the BSTO. The multiple peaks observed in the pattern are well indexed to the hexagonal $BaTa_2O_6$ (i.e., BTO) and $BaSb_2O_6$ (i.e., BSO) phases. The peaks indexed in black and blue are of BTO and BSO phases, respectively. Most of the peaks are assigned to the hexagonal $BaTa_2O_6$ and $BaSb_2O_6$ phases with the space groups of P6/mmm (JCPDS No.74–1321) and P-31 m (JCPDs No. 46–1494), respectively. The BTO hexagonal structure constituted of co-ordination of Ta with octahedral oxygen rings with corner and edge-sharing in the sheet-like pattern, and the Ba atom located at interstitial sites [30]. The BSO phase composed of infinite sheets of $(SbO_6)^{2-}$ octahedra with alternating layers of Ba^{2+}[31] is akin to the crystal structure of BTO but only differs in the 3, 5, and 6 membered oxygen rings. However, the interchangeability between the hexagonal BTO and BSO phase in the entire crystal system may not be feasible due to their space group variation. Apart from this, two unindexed peaks observed at 38.6° and 42.1° are assigned to (202) and (212) planes of the Ta suboxide phase (i.e., TaO_x) [32]. The dramatically reduced intensity of these peaks indicates the insignificant presence of the TaO_x phase in the BSTO. Overall, the XRD analysis confirms that the prepared compound has arranged in the general formula of $Ba(Sb/Ta)_2O_6$ with minor traces of the TaO_xphase.

The electronic structure and the chemical oxidation states of the BSTO are performed using *X*-ray photoelectron spectroscopy (XPS). Fig. 3 shows the XPS spectra of core levels of Ba(3d), Ta(4f), Sb(3d), and O(1s) present in the BSTO. All the spectra are deconvoluted via the Voigt curve fitting function with the Shirley background. The double peak feature of Ba(3d) core levels is perfectly fitted with two peaks located (Fig. 3(a)) at binding energy (BE) of 780.2 and 795.6 eV representing the core levels of $Ba^{2+}(3d_{5/2})$ and $B^{2+}(3d_{3/2})$, respectively [33]. The energy separation of 15.4 eV observed between $Ba(3d_{5/2})$ and $Ba(3d_{3/2})$ is assigned to the Ba^{2+} oxidation state. Moreover, the XPS spectra of the Ta(4f) core levels of BSTO shows two distinct peaks identified as 'a' and 'b' located at BE of 25.9 and 27.8 eV (Fig. 3(b)), which represents the core level of the $Ta(4f_{7/2})$, and $Ta(4f_{5/2})$, respectively. The deconvolution of spectra illustrates a perfect fit for four peaks identified as a', a, b', and b, which are located at 25.2, 25.9, 27.4, and 27.8 eV, respectively. The peaks located at BE of 25.9 (≡ a), and 27.8 (≡ b), eV, corresponds to the $Ta(4f_{7/2})$ and $Ta(4f_{5/2})$ core level of 5+ cations [34–37] in BSTO. However, the other two weak intensity peaks observed in co-occurrence and located at BE of 25.2 (≡ a') and 27.4 (≡ b') eV are of the $Ta(4f_{7/2})$ and $Ta(4f_{5/2})$ core level of sub oxidized (i.e., < 4+ cations) Ta form in BSTO. Moreover, the energy separation of 1.9 eV estimated between the $Ta(4f_{7/2})$ (≡ a) and $Ta(4f_{5/2})$ (≡ b) is assigned to the Ta^{5+} oxidation state, and 2.1 eV observed in the other two concurrent peaks is allotted to the suboxidized form of Ta (i.e., TaO_x). Moreover, the 9-fold higher intensity of Ta^{5+}(4f) peaks (i.e., a and b) than that of sub-oxidized peaks (i.e., a' and b') specifies the presence of very minute amount of suboxides phases of the Ta (i.e., TaO_x). Likewise, Fig. 3(c) shows the perfect fit for three distinct peaks located at BE of 530.2, 531.9, and 540.1 eV. The peaks at BE of 530.2 and 540.1 eV correspond to the $Sb(3d_{5/2})$ and $Sb(3d_{3/2})$ core levels of 5+ cations [38] in the BSTO. Moreover, the energy separation of 9.9 eV observed between the $Sb(3d_{5/2})$ and $Sb(3d_{3/2})$ core levels is akin to that identified for the Sb^{5+} oxidation state [39]. The peak at BE of 531.9 eV represents the O(1 s) core level of 2- anions [40–43], where the peak assigned to surface contamination is not accompanied by O(1 s) indicates the formation of oxidized BSTO phase. The utilization of $SbCl_3$ precursor was expected to provide the Sb^{3+} oxidation state for the formation of double perovskite BSTO, but the presence of the Sb^{5+} chemical state along with the Ta-suboxide phase confirms the evolution of the most stable Ba $(Sb/Ta)_2O_6$ phase. This observation is akin to the XRD and TEM analysis detailed above.

UV–Vis spectra of BSTO was recorded to understand the photon dependent absorption behavior. The diffuse reflectance spectrum of BSTO was obtained using an integrated sphere detector assembly with pure $BaSO_4$ powder as a reference. The diffused reflectance

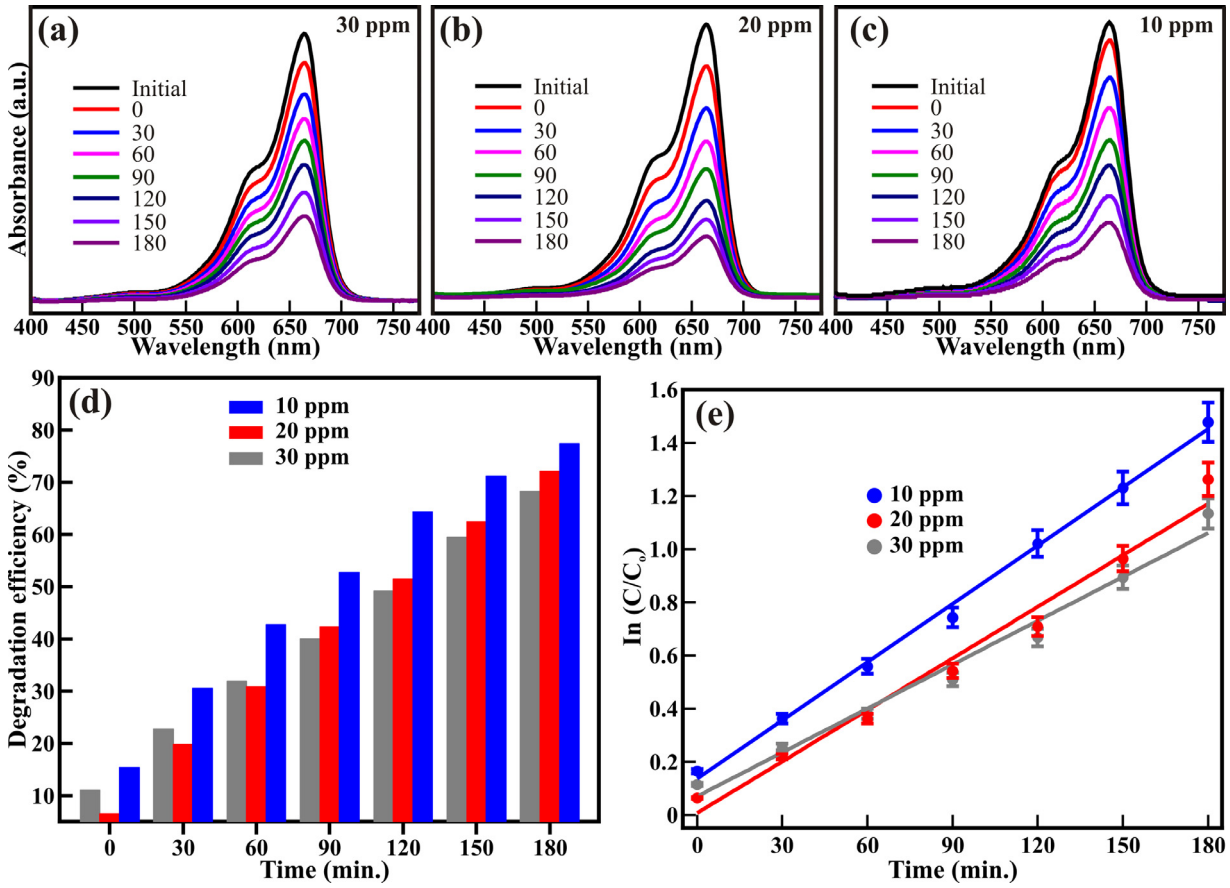

Fig. 4. UV-Visible absorption spectra gained at regular time intervals for photocatalytic degradation of (**a**) 30, (**b**) 20, and (**c**) 10 ppm MB dye solution adopting BSTO perovskite catalyst. Irradiation time-dependent (**d**) histogram of degradation efficiency, and (**e**) photocatalytic decomposition rate estimated for photocatalytically reduced MB adopting BSTO perovskite.

spectra (DRS) plotted in Fig. S2 is obtained by referring to the Kubelka-Munk function, [17] $F(r) = A(h\nu\text{-}E_g)^{m/2}$, Where, m is constant defined from the optical transition of the material, E_g is the bandgap of material, and hv is photon energy. The extrapolation of the DRS spectrum illustrated a bandgap of 3.48 eV, which is akin to the values reported for the BTO and BSO [12,18,21,22]. This indicates that the UV-active BSTO has the ability to deliver the collective effect of BTO and BSO and enhance photocatalytic activities.

The various organic dyes were utilized to understand the photocatalytic dye-degradation mechanism of the BSTO. The photocatalytic reaction mechanism was optimized on the MB. Fig. 4(a–c) shows the UV–Vis spectra recorded after the photocatalytic reaction of different amounts of MB for various reaction times. Initial optimization was performed on 10, 20, and 30 ppm MB solutions while utilizing 25 mg of BSTO. The intense absorption peak at 664 nm, accompanied by a shoulder peak at 612 nm, corresponds to the MB dyes [44] was observed after adsorption-desorption equilibrium (i.e., initial state). Another absorption peak is not observed, confirm that no intermediate reaction has happened to form dye-complexes. Fig. 4(a) shows the absorption spectra recorded at different time intervals for the photocatalytic reaction of 30 ppm MB. The absorption peak intensity is inversely proportional to the photocatalytic reaction time. The peak intensity of λ_{max} decreased without any shifting in the peak position. This illustrates that the dye has not formed any complexes but degraded photocatalytically with an increase in the irradiation or reaction time. Moreover, Fig. 4(b) and (c) illustrate explicitly identical absorption behavior after photocatalytic reaction observed for 20 and 10 ppm MB solution, respectively. Further, to evaluate the performance of BSTO in the photocatalytic degradation of different concentrations of MB dye, the dye degradation efficiency calculated from [45]

$$\%\ \text{degradation} = (1 - C/C_o) \times 100 \quad (1)$$

Where, C_o is the absorbance (i.e., initial dye concentration) before exposure to light (i.e., $t = 0$), and C is a change in absorbance (i.e., dye concentration) after exposure to light ($t = t$).

Fig. 4(d) shows the histogram of the MB dye degradation at different time intervals estimated from the absorption spectra. The degradation efficiency of the BSTO catalyst has increased with an increase in the photocatalytic reaction time, and maximum values are obtained after 180 min. irrespective of the concentration of MB dye. The best degradation efficiency of 77.3, 72.1, and 68.2% was achieved for 10, 20, and 30 ppm MB after 180 min photocatalytic reaction with BSTO. Thus, the highest degradation efficiency of 77.3% was obtained for 10 ppm MB dye after a photocatalytic reaction of 180 min.

Further, we have explored the kinetics of the photocatalytic reduction of MB utilizing BSTO. The linear variation in the $\ln(C/C_o)$ with respect to the photocatalytic reaction time reveals the pseudo-first-order reaction kinetics. The pseudo-first-order contact (k) was evaluated from the equation [46].

$$ln(C/C_o) = -kt \quad (2)$$

Where, C_o and C are the absorbances at time $t = 0$ (i.e., initial dye concentration) and $t = t$ (i.e., dye concentration after exposure), respectively, and k is the reaction rate constant at a time interval of t (i.e., /min.). Fig. 4(e) illustrates the photocatalytic reaction time-dependent linear variation in the $\ln(C/C_o)$ of various MB concentrations. The k values of 0.0073, 0.0065, and 0.0055 /min. were observed for a reduction of 10, 20, and 30 ppm MB. The larger rate constant value is observed for 10 ppm MB than 20 and 30 ppm concentration.

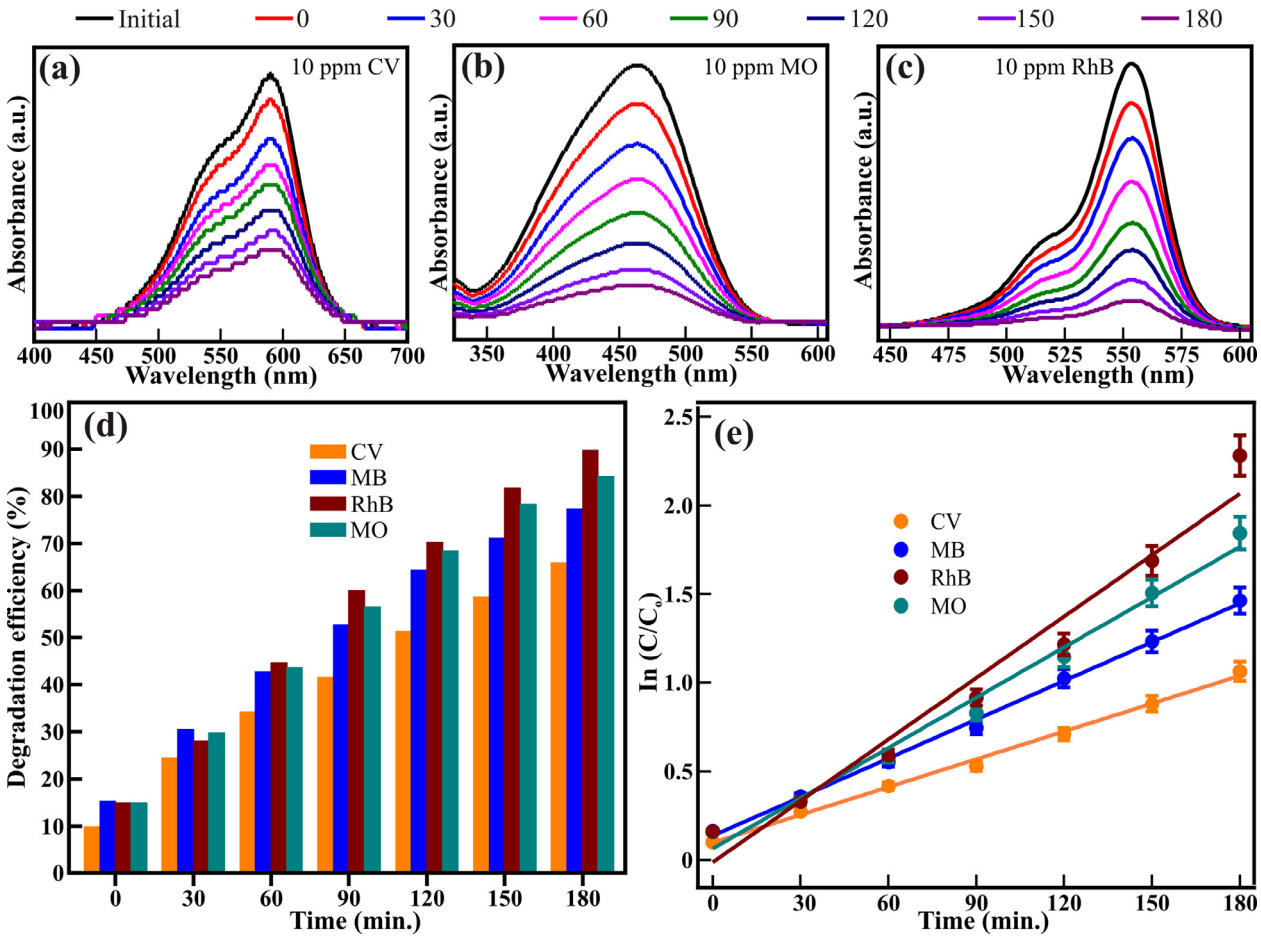

Fig. 5. UV-Visible absorption spectra gained at regular time intervals for photocatalytic degradation of 10 ppm (**a**) CV, (**b**) MO, and (**c**) RhB dyes solution adopting BSTO perovskite catalyst. Irradiation time-dependent (**d**) histogram of degradation efficiency, and (**e**) photocatalytic decomposition rate estimated for photocatalytically reduced CV, MB, RhB, and MO employing BSTO perovskite.

Moreover, the correlation coefficient (R^2) estimated was 0.996, 0.977, and 0.976, respectively. The saturation of dye solution on the catalyst surface leads to a decrease in the active reaction sites, which might be one reason behind this [47]. Moreover, the decreased penetration of light reflects the reduction of photocatalytic efficiency. We have performed further photocatalytic degradation studies on the 10 ppm concentration of various dyes in view of these observations.

Fig. 5(a–c) shows the UV–Vis spectra recorded after photocatalytic reaction of 10 ppm CV, MO, and RhB for different reaction times. The intense absorption peaks at 590, 464, and 554 nm corresponds to the CV (Fig. 5(a)), MO (Fig. 5(b)) and RhB (Fig. 5(c)) dyes, respectively, [45,48] observed after adsorption-desorption equilibrium (i.e., initial state). The nonappearance of other absorption peaks in the spectra confirms that the intermediate reaction has not formed dye-complexes. The intensity of the absorption peaks (λ_{max}) for all dyes has decreased with an increase in the photocatalytic reaction time, and the peak position (i.e., λ_{max}) has not shifted at all for CV, MO, and RhB. This corroborates that all dyes have degraded photocatalytically without forming any complexes even after increasing the irradiation time.

Fig. 5(d) shows the histogram of all studied dyes degradation efficiency estimated from the absorption spectra collected at different intervals. The time-dependent degradation behavior of the BSTO catalyst for 10 ppm CV, MO, and RhB is akin to that for MB dye. Although BSTO delivered better efficiency for the degradation of MB and MO dyes initially (i.e., < 60 min.), a better degradation response was observed for RhB after irradiation for 180 min. The degradation efficiency observed for CV, MB, RhB, and MO dyes is 65.9%, 77.3%, 89.8%, 84.2%, respectively, after 180 min. irradiation in the presence of BSTO. This specifies that the BSTO shows good photocatalytic degradation activities for CV, MB, RhB, and MB dyes. However, the maximum efficiency of 89.8% gained for 10 ppm RhB after 180 min. photocatalytic irradiation confirmed the excellent photocatalytic behavior towards RhB. Fig. 5(e) shows the irradiation time-dependent linear variation in the ln(C/C_o) of all studied dyes and revealed the pseudo-first-order reaction kinetics similar to the MB. The k values of 0.0052, 0.0073, 0.0115, and 0.0095 /min. were calculated for a reduction of 10 ppm CV, MB, RhB, and MO, respectively. The BSTO delivered a higher rate constant for RhB and a lower rate constant for CV dye. Moreover, the correlation coefficient (R^2) for CV, MB, RhB, and MO was 0.995, 0.996, 0.958, and 0.985, respectively. This depicts the better response of BSTO for the photocatalytic removal of 10 ppm RhB than that of CV, MO, and MB dyes.

The photocatalytic stability of the BSTO perovskites for the reduction of organic dyes is confirmed from cyclic studies. Fig. S3 shows the cyclic stability of BSTO perovskite during the photocatalytic reduction of RhB. BSTO has shown stable behavior without significant loss in photocatalytic activities for three continuous cycles of 570 min. The ~ 7% reduction witnessed after the third cycle might be due to the weight loss of BSTO during the recovery process. This proves the substantial stable photocatalytic cyclability of BSTO perovskite in the removal of organic dyes.

Considering that the formation of O_2^- and OH^-surface radicals play an important role in the degradation of the dyes; we have carried out systematic DFT calculations to unravel the adsorption mechanism of O_2 and H_2O species on the BSTO(100) surface. The optimized bulk

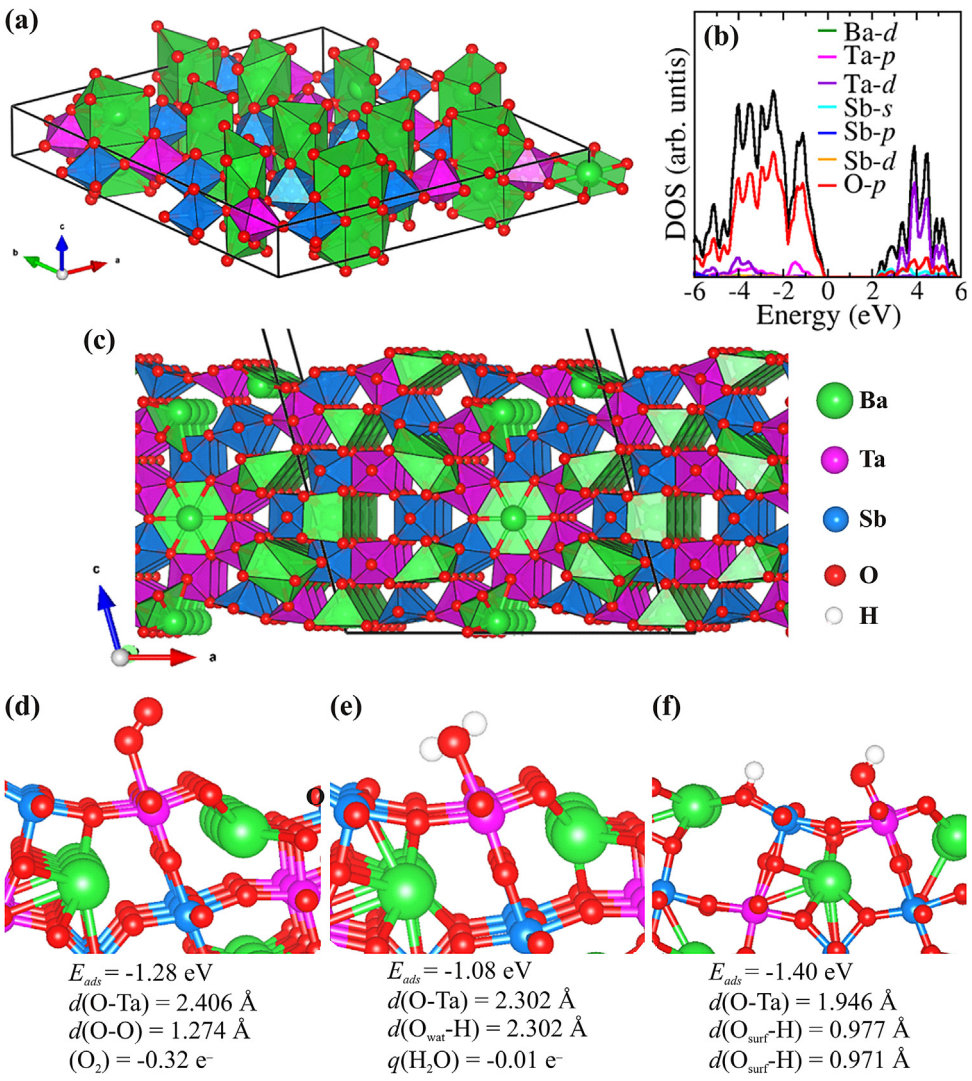

Fig. 6. (**a**) Optimized structure of hexagonal BSTO in a polyhedral form, (**b**) corresponding projected density of states, and (**c**) the surface structure of the (100) surface. Optimized structures of the lowest-energy adsorption geometries of (**d**) O_2, (**e**) molecular H_2O, and (**f**) dissociated H_2O on BSTO (100) surface.

structure of BSTO in polyhedron form is shown in Fig. 6(a), and the corresponding electronic structure, as well as the surface structure of the (100) surface, is shown in Fig. 6(b,c), respectively, predicting a bandgap of 2.15 eV. The difference in the experimental (i.e., 3.48 eV) and theoretical predicted (i.e., 2.15 eV) bandgap values might have resulted from the reduced nanoscale dimensions of hexagonal and irregular shaped particles over the bulk dimensions considered for DFT analysis. The valence band is dominated by O-*p* states, whereas the conduction band edge is dominated by Sb-*s* and O-*p* states. Ta-*p* states have contributions close to the valence band between −1.0 and −2.0 eV. Different adsorption sites (Ba, Ta, and Sb) were explored for the O_2 and H_2O molecules to predict the lowest energy adsorption geometries reported in Fig. 6(d–f). Generally, the Ta sites are found to be more reactive towards both O_2 and H_2O adsorption. The adsorption of O_2 released adsorption energy of 1.28 eV, with the *O*–Ta, predicted at 2.406 Å (Fig. 6(d)). The O − O bond distances are calculated at 1.274 Å, indicating elongation O − O bond relative to the gas phase O_2 molecule (1.24 Å). The adsorption of the O_2 molecule is characterized by a charge transfer of 0.32 e^- as estimated from Bader population analysis, suggesting the formation of O_2^- radicals. Molecular H_2O release an adsorption energy of 1.08 eV, compared to 1.40 eV for dissociated H_2O (H + OH pair) adsorption (Fig. 6 (e,f)). These results suggest that the BSTO(100) surface will promote the dissociation of H_2O to form surface OH^- radicals. The O_2^- and OH^- radicals formed on the BSTO(100) surface are expected to react with the studied dyes, facilitating their degradation.

The distinct scavengers like methanol (MeOH), ammonium oxalate (AO), and isopropanol (IPA) were employed to reveal the impact of superoxide radicals ($\cdot O_2^-$) photogenerated holes (H^+), and hydroxyl radicals ($\cdot OH$) respectively, in the photocatalytic degradation of organic dyes [49]. Fig. 7(a) shows the photocatalytic reduction of RhB in the presence of MeOH, AO, and IPA. IPA revealed a more significant quenching in photocatalytic degradation of RhB and endorsed the dominance of hydroxyl radicals ($\cdot OH$) in the photodegradation process. Moreover, a substantial decrease in the degradation efficiency in the presence of AO indicating the effectiveness of H^+ -in this process. The modest drop in the degradation efficiency for MeOH suggests the partial contribution of $\cdot O_2^-$. Thus, the photogenerated OH^-, and H^+ from BSTO perovskite are substantially stimulating the photocatalytic reduction of organic dyes. Based on these results, the possible degradation mechanism for dyes adsorbed on the catalyst surface is shown in Fig. 7(b). The irradiation of BSTO under xenon lamp transfers photogenerated electrons (e^-) to the conduction band (CB), leaving holes (h^+) in the valance band (VB). The hydroxyl groups at the catalyst surface trap these holes and yield the hydroxyl radicals ($\cdot OH$). However, electrons at CB produces $\cdot O_2^-$ radicles after reacting with

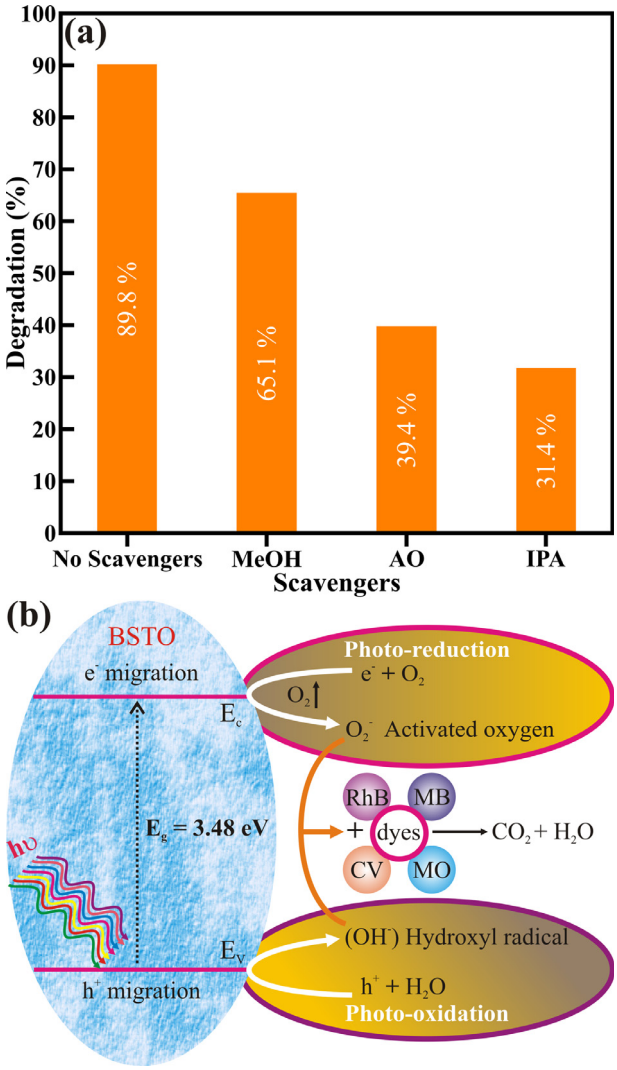

Fig. 7. (a) Effect of distinct scavengers on the photoreduction of RhB using BSTO perovskite, (b) schematic illustration of the photocatalytic mechanism of BSTO in the degradation of organic dyes.

dissolved oxygen molecule and further produce hydroxide radicals ($HO_2^{\cdot}$) after protonation [50,51]. These radicals dissociate the dyes into nontoxic compounds. The larger accessible surface area, the bandgap of 3.48 eV, and largely accessible surface free-electron provide a larger number of photogenerated e^-–h^+ pairs to boost the photocatalytic activities of BSTO. Therefore, the following photocatalytic reactions are expected for BSTO,

$$2\,\mathrm{BSTO} + h\nu \rightarrow \mathrm{BSTO}\,(e^- + h^+) \quad (3)$$

$$\mathrm{BSTO}\,(h^+) + H_2O \rightarrow H^+ + {}^{\cdot}OH + \mathrm{BSTO} \quad (4)$$

$$\mathrm{BSTO}\,(e^-) + O_2 \rightarrow \mathrm{BSTO} + {}^{\cdot}O_2^- \quad (5)$$

$$\mathrm{BSTO}\,(h^+) + OH^- \rightarrow {}^{\cdot}OH + \mathrm{BSTO} \quad (6)$$

$$\mathrm{BSTO}\,(e^-) + {}^{\cdot}O_2^- + H^+ \rightarrow HO_2^{\cdot} + \mathrm{BSTO} \quad (7)$$

$$HO_2^{\cdot} + H^+ \rightarrow H_2O_2 \quad (8)$$

$$H_2O_2 + e^- \rightarrow {}^{\cdot}OH + OH^- \quad (9)$$

$$\mathrm{Dye} + {}^{\cdot}OH \rightarrow CO_2 + H_2O \quad (10)$$

Where, the light of sufficient photon energy (i.e., $h\nu > E_{g(BSTO)}$) incident on BSTO would generate e^-–h^+ pairs in the CB and VB, respectively (Eq. (3)). The sensitized H_2O and O_2 molecules on the surface of BSTO trap holes and electrons to form hydroxyl ($^{\cdot}OH$) (Eq. (4)) and superoxide ($^{\cdot}O_2^-$) (Eq. (5)) radicals, respectively. BSTO form $^{\cdot}OH$ radicals in the presence of H^+ ions (Eq. (6)) and further protonated to form H_2O_2 (Eq. (8)). The H_2O_2 traps the e^- and gives $^{\cdot}OH$ radical (Eq. (9)). Moreover, the trapping of e^- enhances the formation of $HO_2^{\cdot}$ radicals (Eq. (7)), which further assists in the protonated formation of H_2O_2 and subsequently to $^{\cdot}OH$ radicals. The $^{\cdot}OH$ radicals act as capable oxidizing agents to significantly degrade the dye pollutants ultimately into H_2O and CO_2. (Eq. (10)). The more significant generation of $^{\cdot}OH$ radicals boosts the degradation of the dye through further oxidation. These observations are akin to our theoretical DFT predictions. The presence of more number of alkyl groups in CV than others constrains the dye solubility in water, which hampers photocatalytic degradation. Likewise, the SO_3^- withdrawing group containing dye like MO shows less reactivity towards photocatalysis. We observed the best degradation rate of BSTO towards RhB dye, which might be owing to the presence of a carboxyl group, unlike in MB [52]. Overall, the perfect crystalline nature, lower bandgap, and largely accessible surface electrons of BSTO have resulted in the admirable photocatalytic degradation of organic dyes.

4. Conclusions

In conclusion, we have observed excellent photocatalytic activity of BSTO towards the degradation of various dyes. FESEM analysis confirms the formation of closely packed 2D hexagonal plates accompanied by clustered nanoparticles of BSTO. XPS evidenced the presence of Ba^{2+}, Sb^{5+}, Ta^{5+}, and O^{2-} oxidation states and revealed the formation of $Ba(Sb/Ta)_2O_6$ phase with minor traces of TaO_x. The DRS revealed a bandgap of 3.48 eV for the BSTO perovskite phase. BSTO exhibited excellent photocatalytic activity for the degradation of various organic dyes. The kinetic studies of BSTO delivered photocatalytic degradation efficiency of 65.9%, 77.3%, 89.8%, and 84.2%, for the CV, MB, RhB, and MO, respectively, after irradiation of 180 min without using cocatalyst. The high ordered reaction rate of pseudo-first-order reaction kinetics indicates the excellent photocatalytic activity of BSTO. Overall, the utilization of BSTO can serve for the photocatalytic degradation of various organic dyes and may be beneficial for chemical transformation, observing the economic, environmental, and safety issues.

Declaration of Competing Interest

The authors declare that they have no known competing financial interests or personal relationships that could have appeared to influence the work reported in this paper.

Acknowledgment

The authors would like to thank TARE-SERB-DST India and UGC-DAE CSR Indore for their financial support to this research under grant No. TAR/2019/000106 and CSR-IC-BL-65/CRS-182/2017–18/189, respectively. SRR and NYD acknowledge the UK Engineering and Physical Sciences Research Council (EPSRC) for funding (Grant No. EP/S001395/1). This work has also used the computational facilities of the Advanced Research Computing, Cardiff (ARCCA) Division at Cardiff University and HPC Wales, This work also utilize the facilities of ARCHER (http://www.archer.ac.uk), the UK's national supercomputing service via the membership of the HEC Materials Chemistry Consortium funded by EPSRC (EP/L000202). Information on the data that underpins the results presented here, including how to access them, can be found in the Cardiff University data catalogue at http://doi.org/10.17035/d.2021.0133743636.

Supplementary materials

Supplementary material associated with this article can be found, in the online version, at doi:10.1016/j.jtice.2021.04.032.

References

[1] González P, Zaror C, Carrasco V, Mondaca M, Mansilla H. Combined physical-chemical and biological treatment of poorly biodegradable industrial effluents. J Environ Sci Health A 2003;38:2201–8.
[2] Piaskowski K, Swiderska D, Zarzycki P. Dye removal from water and wastewater using various physical, chemical, and biological processes. J AOAC Int 2018;101:1371–84.
[3] Anwer H, Mahmood A, Lee J, Kim K, Park J, Yip A. Photocatalysts for degradation of dyes in industrial effluents: opportunities and challenges. Nano Res 2019;12:955–72.
[4] Nakata K, Ochiai T, Murakami T, Fujishima A. Photoenergy conversion with TiO_2 photocatalysis: new materials and recent applications. Electrochim Acta 2012;84:103–11.
[5] Dong HR, Zeng GM, Tang L, Fan CZ, Zhang C, He XX, He Y. An overview on limitations of TiO_2-based particles for photocatalytic degradation of organic pollutants and the corresponding countermeasures. Water Res 2015;79:128–46.
[6] Schneider J, Matsuoka M, Takeuchi M, Zhang J, Horiuchi Y, Anpo M, Bahnemann DW. Understanding TiO_2 photocatalysis: mechanisms and materials. Chem Rev 2014;114:9919–86.
[7] Kohtani S, Hiro J, Yamamoto N, Kudo A, Tokumura K, Nakagaki R. Adsorptive and photocatalytic properties of Ag-loaded $BiVO_4$ on the degradation of 4-*n*-alkylphenols under visible light irradiation. Catal Commun 2005;6:185–9.
[8] Alaoui OT, Nguyen QT, Mbareck C, Rhlalou T. Elaboration and study of poly(vinylidene fluoride)-anatase TiO_2 composite membranes in photocatalytic degradation of dyes. Appl Catal A Gen 2009;358:13–20.
[9] Salem MA, Al-Ghonemiy AF, Zaki AF. Photocatalytic degradation of allura red and quinoline yellow with polyaniline/TiO_2 nanocomposite. Appl Catal B Environ 2009;91:59–66.
[10] An XQ, Yu JC. Graphene-based photocatalytic composites. RSC Adv 2011;1:1426–34.
[11] Kanhere P, Chen Z. A review on visible light active perovskite-based photocatalysts. Molecules 2014;19:19995–20022.
[12] Kim NG, Avdeev M, Kim YI. Tunnel structure of tetragonal tungsten bronzes $BaTa_2O_6$, $Ba_{0.8}Ta_2O_{5.8}$, and $Ba_{0.5}Ta_2O_{5.5}$ studied using synchrotron *X*-ray and neutron diffraction. J Alloy Compd 2020;815:152420.
[13] Xu TG, Zhang C, Shao X, Wu K, Zhu YF. Monomolecular-layer $Ba_5Ta_4O_{15}$ nanosheets: synthesis and investigation of photocatalytic properties. Adv Funct Mater 2006;16:1599–607.
[14] Xu TG, Zhao X, Zhu YF. Synthesis of hexagonal $BaTa_2O_6$ nanorods and influence of defects on the photocatalytic activity. J Phys Chem B 2006;110:25825–32.
[15] Kudo A, Yoshino S, Tsuchiya T, Udagawa Y, Takahashi Y, Yamaguchi M, Ogasawara I, Matsumoto H, Iwase A. Z-scheme photocatalyst systems employing Rh- and Ir-doped metal oxide materials for water splitting under visible light irradiation. Faraday Discuss 2019;215:313–28.
[16] Chen J, Li DZ, Wang JB, Wang P, Cao CS, Shao Y, Wang JX, Xian JJ. Morphological effect on photocatalytic degradation of Rhodamine B and conversion of active species over $BaSb_2O_6$. Appl Catal B Environ 2015;163:323–9.
[17] Dutta DP, Ballal A, Singh A, Fulekar MH, Tyagi AK. Multifunctionality of rare earth doped nano $ZnSb_2O_6$, $CdSb_2O_6$ and $BaSb_2O_6$: photocatalytic properties and white light emission. Dalton Trans 2013;42:16887–97.
[18] Chen J, Li DZ, Hu JH, Chen W, Wang JX, Hu Y, Fu XZ, Shao Y. One-step template-free synthesis of $BaSb_2O_6$ micro-flowers and their associated photocatalytic activity. CrystEngComm 2012;14:8382–9.
[19] Iwase A, Kudo A. Development of Ir and La-codoped $BaTa_2O_6$ photocatalysts using visible light up to 640 nm as an H_2-evolving photocatalyst for Z-schematic water splitting. Chem Commun 2017;53:6156.
[20] Hatakeyama T, Takeda S, Ishikawa F, Ohmura A, Nakayama A, Yamada Y, Matsushita A, Yea J. Photocatalytic activities of Ba_2RBiO_6 (R = La, Ce, Nd, Sm, Eu, Gd, Dy) under visible light irradiation. J Ceram Soc Jpn 2010;118:91–5.
[21] Soldat J, Marschall R, Wark M. Improved overall water splitting with barium tantalate mixed oxide composites. Chem Sci 2014;5:3746–52.
[22] Mizoguchi H, Woodward PM. Electronic structure studies of main group oxides possessing edge-sharing octahedra: implications for the design of transparent conducting oxides. Chem Mater 2004;16:5233–48.
[23] Kresse G, Furthmüller J, Hafner J. Theory of the crystal structures of selenium and tellurium: the effect of generalized-gradient corrections to the local-density approximation. Phys Rev B 1994;50:13181–5.
[24] Blöchl PE. Projector augmented-wave method. Phys Rev B 1994;50:17953–79.
[25] Perdew JP, Burke K, Ernzerhof M. Generalized gradient approximation made simple. Phys Rev Lett 1997;78 1396-1396.
[26] Grimme S, Antony J, Ehrlich S, Krieg H. A consistent and accurate ab initio parametrization of density functional dispersion correction (DFT-D) for the 94 elements H-Pu. J Chem Phys 2010;132:154104.
[27] Mumme WG, Grey IE, Roth RS, Vanderah TA. Contrasting oxide crystal chemistry of Nb and Ta: The structures of the hexagonal bronzes $BaTa_2O_6$ and $Ba_{0.93}Nb_{2.03}O_6$. J Solid State Chem 2007;180:2429–36.
[28] Krukau AV, Vydrov OA, Izmaylov AF, Scuseria GE. Influence of the exchange screening parameter on the performance of screened hybrid functionals. J Chem Phys 2006;125:224106.
[29] Tang W, Sanville E, Henkelman G. A grid-based Bader analysis algorithm without lattice bias. J Phys Condes Matter 2009;21:084204.
[30] Gk Layden. Dielectric and structure studies of hexagonal $BaTa_2O_6$. Mater Res Bull 1968;3:349–59.
[31] DeBoer BG, Young RA, Sakthivel A. *X*-ray Rietveld structure refinement of Ca, Sr and Ba meta-antimonates. Acta Crystallogr C 1994;50:476–82.
[32] Zhou YM, Xie Z, Xiao HN, Hu PF, He J. Structure and properties of Ta/TaO_x barrier films deposited by direct current magnetron sputtering. Vacuum 2009;84:330–4.
[33] Keswani BC, Devan RS, Kambale RC, James AR, Manandhar S, Kolekar YD, Ramana CV. Correlation between structural, magnetic and ferroelectric properties of Fe-doped (Ba-Ca)TiO_3 lead-free piezoelectric. J Alloy Compd 2017;712:320–33.
[34] Devan RS, Ho W, Chen CH, Shiu HW, Ho CH, Cheng CL, Wu SY, Liou Y, Ma YR. High room-temperature photoluminescence of one-dimensional Ta_2O_5 nanorod arrays. Nanotechnology 2009;20:445708.
[35] Devan RS, Ho WD, Lin JH, Wu SY, Ma YR, Lee PC, Liou Y. *X*-ray diffraction study of a large-scale and high-density array of one-dimensional crystalline tantalum pentoxide nanorods. Cryst Growth Des 2008;8:4465–8.
[36] Devan RS, Lin CL, Gao SY, Cheng CL, Liou Y, Ma YR. Enhancement of green-light photoluminescence of Ta_2O_5 nanoblock stacks. Phys Chem Chem Phys 2011;13:13441–6.
[37] Devan RS, Lin JH, Ho WD, Wu SY, Liou Y, Ma YR. Investigation of high-temperature phase transformation in one-dimensional Ta_2O_5 nanorods. J Appl Crystallogr 2010;43:1062–7.
[38] Annamalai A, Sandstrom R, Gracia-Espino E, Boulanger N, Boily JF, Muhlbacher I, Shchukarev A, Wagberg T. Influence of Sb^{5+} as a double donor on hematite (Fe^{3+}) photoanodes for surface-enhanced photoelectrochemical water oxidation. ACS Appl Mater Interfaces 2018;10:16467–73.
[39] Djieutedjeu H, Zhou XY, Chi H, Haldolaarachchige N, Ranmohotti KGS, Uher C, Young D, Poudeu PFP. Donor and acceptor impurity-driven switching of magnetic ordering in $MnSb_{2-x}Sn_xSe_4$. J Mater Chem C 2014;2:6199–210 2.
[40] Chikate PR, Daware KD, Gayhane DS, Ma YR, Choudhary RJ, Patil SI, More MA, Phase DM, Gosavi SW, Shirage PM, Devan RS. Controlled hetero-architectures of Au-nanoparticles-decorated ZnO nanowires for enhanced field electron emission displays. ChemistrySelect 2018;3:7891–9.
[41] Chikate PR, Daware KD, Patil SS, Didwal PN, Lole GS, Choudhary RJ, Gosavi SW, Devan RS. Effects of Au loading on the enhancement of photoelectrochemical activities of the Au@ZnO nano-heteroarchitecture. New J Chem 2020;44:5535–44.
[42] Kitchamsetti N, Kalubarme RS, Chikate PR, Park CJ, Ma YR, Shirage PM, Devan RS. An investigation on the effect of Li-Ion cycling on the vertically aligned brookite TiO_2 nanostructure. Chem Select 2019;4:6620–6.
[43] Kitchamsetti N, Ma YR, Shirage PM, Devan RS. Mesoporous perovskite of interlocked nickel titanate nanoparticles for efficient electrochemical supercapacitor electrode. J Alloy Compd 2020;833:155134.
[44] Balu S, Uma K, Pan GT, Yang TCK, Ramaraj SK. Degradation of methylene blue dye in the presence of visible light using SiO_2@-Fe_2O_3 nanocomposites deposited on SnS_2 flowers. Materials 2018;11:1030. (Basel).
[45] Hernandez-Gordillo A, Bizarro M, Gadhi TA, Martinez A, Tagliaferro A, Rodil SE. Good practices for reporting the photocatalytic evaluation of a visible-light active semiconductor: Bi_2O_3, a case study. Catal Sci Technol 2019;9:1476–96.
[46] Tangcharoen T, T-Thienprasert J, Kongmark C. Optical properties and versatile photocatalytic degradation ability of MAl_2O_4 (M = Ni, Cu, Zn) aluminate spinel nanoparticles. J Mater Sci Mater Electron 2018;29:8995–9006.
[47] Rashmi SK, Naik HSB, Jayadevappa H, Viswanath R, Patil SB, Naik MM. Solar light responsive Sm-Zn ferrite nanoparticle as efficient photocatalyst. Mater Sci Eng B Adv Funct Solid State Mater 2017;225:86–97.
[48] Taniguchi M, Lindsey JS. Database of absorption and fluorescence spectra of > 300 common compounds for use in photochem CAD. Photochem Photobio 2018;94:290–327.
[49] Kitchamsetti N, Ramteke MS, Rondiya SR, Mulani SR, Patil MS, Cross RW, Dzade NY, Devan RS. DFT and experimental investigations on the photocatalytic activities of NiO nanobelts for removal of organic pollutants. J Alloy Compd 2020:157337.
[50] Martinez-de la Cruz A, Perez UMG. Photocatalytic properties of $BiVO_4$ prepared by the co-precipitation method: degradation of rhodamine B and possible reaction mechanisms under visible irradiation. Mater Res Bull 2010;45:135–41.
[51] Zhang LL, Long JX, Pan WW, Zhou SY, Zhu JW, Zhao YJ, Wang X, Cao GZ. Efficient removal of methylene blue over composite-phase $BiVO_4$ fabricated by hydrothermal control synthesis. Mater Chem Phys 2012;136:897–902.
[52] Julkapli N, Bagheri S, Abd Hamid SB. Recent advances in heterogeneous photocatalytic decolorization of synthetic dyes. Sci World J 2014:692307.